Ultrasonics 158 (2026) 107831

Contents lists available at ScienceDirect

Ultrasonics

journal homepage: www.elsevier.com/locate/ultras

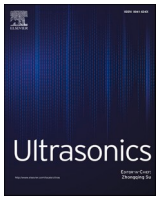

Cost-effective laser diode scanning 3D photoacoustic microscopy of melanocytic dermal tumors in situ

Javier A. Navarro-Calvo [a], Alejandro Cebrecos [a], Adrián Arándiga [a], Laura Lorenzo-Rebenaque [b], Francisco Marco-Jiménez [b], José M. Benlloch [a], Francisco Camarena [a], Juan J. García-Garrigós [a,*]

[a] Instituto de Instrumentación para Imagen Molecular, Consejo Superior de Investigaciones Científicas - Universitat Politècnica de València, 46022 Valencia, Spain
[b] Instituto de Ciencia y Tecnología Animal, Universitat Politècnica de València, 46022 Valencia, Spain

ARTICLE INFO

Keywords:
Laser diode scanning
Cost-effective 3D photoacoustic microscopy
Melanoma imaging
Point of care

ABSTRACT

Management of melanoma skin cancer involves a wide excision followed by histopathological analysis to confirm the diagnosis, which is only guided by superficial dermoscopy. Dermatological oncology can thus benefit from high-resolution, 3D images provided by photoacoustic microscopy; however, its clinical translation is hindered by its elevated cost. Opening a pathway to point-of-care 3D melanoma assessment, we present the first demonstration of a cost-effective photoacoustic microscope (CePAM) utilizing fast laser diode scanning with a focused transducer in reflection mode. A novel application of a direct model inversion (DiMI) algorithm allowed a 55-fold enlargement of the image field of view beyond the transducer acoustic focus, reaching a 1-square millimeter laser-scanned area with uniform sensitivity (>20 dB). Furthermore, DiMI improved the intrinsic axial resolution of the system via multiple selective-plane scanning. The feasibility of CePAM is demonstrated by quantitative tests on phantoms and *in vivo* imaging of murine melanocytic dermal tumors, yielding accurate 3D images and virtual cross-sections consistent with histology.

1. Introduction

Photoacoustic (PA) imaging is a cutting-edge biomedical imaging technique with the potential to provide valuable insights into a wide range of medical applications. By leveraging the production of ultrasound waves through the optically selective absorption of laser light into the tissue, PA imaging can generate label-free volumetric images of endogenous chromophores such as hemoglobin and melanin at greater depths than purely optical methods [1,2]. The non-ionizing nature of this medical imaging technique makes it particularly well-suited for frequent, noninvasive monitoring of a wide variety of pathologies [3,4].

Melanocytic dermal tumors (MDT), especially primary cutaneous melanomas, have been an early target for experimental photoacoustic microscopy (PAM) systems [5–9], due to PAM's ability to precisely determine the extent and depth of tumor penetration *in vivo* [10,11]. Melanomas account for the great majority of skin cancer deaths (~90 %) due to their high risk of metastasis which escalates with deeper skin penetration. Consequently, the vertical tumor thickness or Breslow depth [12], is used for tumor staging, ranging from T1 (≤ 1 mm) to T4 (> 4 mm) [13,14]. A recent study demonstrated a high 10-year survival rate of 93 % for thin melanomas < 0.8 mm (T1) [15], but this rate declines significantly to 50 % for T4 tumors, underscoring the need for early detection and frequent monitoring of these aggressive skin tumors [16]. PAM systems have the potential to facilitate early detection of melanoma, a crucial factor in patient outcomes, by providing additional information beyond the visual inspection of moles using conventional dermoscopy [17]. However, the significant cost and size of PAM systems using pulsed nanosecond solid-state lasers (SSLs) has hindered their widespread adoption into standard clinical practice, despite the exceptional imaging performance provided by their high-energy and Gaussian-quality beams [18–20]. Consequently, affordable systems are urgently needed to bring the benefits of this PA technology to patients, especially for melanoma detection. Significantly less expensive and more compact laser diodes (LDs) have been proposed as an alternative

* Corresponding author.
E-mail addresses: janacal@i3m.upv.es (J.A. Navarro-Calvo), alcebrui@i3m.upv.es (A. Cebrecos), adarmar2@i3m.upv.es (A. Arándiga), laulore@upv.es (L. Lorenzo-Rebenaque), fmarco@dca.upv.es (F. Marco-Jiménez), benlloch@i3m.upv.es (J.M. Benlloch), fracafe@fis.upv.es (F. Camarena), jjgarcia@i3m.upv.es (J.J. García-Garrigós).

https://doi.org/10.1016/j.ultras.2025.107831
Received 20 June 2025; Received in revised form 5 September 2025; Accepted 22 September 2025
Available online 25 September 2025

technology in PA scanning microscopy, requiring lower laser pulse energy at high repetition rates. However, low-power, low-quality LD beams typically require a short and tight focusing distance to achieve adequate signal levels and competitive resolutions. As a result, the laser working distance in LD-PAM systems is severely reduced [21–23], posing a challenge to the integration of fast laser scanning mirrors and other key system components in a reflection mode configuration as required for practical *in vivo* imaging and in contrast to SSL-based PAM systems [24–28]. Some previous systems operate in transmission mode for thin tissue imaging, for example, using single-wavelength near-infrared (NIR) pulsed laser diodes (PLD) with relatively high peak power [29–31], or modulating continuous wave (CW) visible laser diodes for multi-wavelength imaging [32]. Recently, newer reflection mode systems have adopted an effective fiber coupling design to homogenize the low-quality LD beams using a NIR-PLD [33], and also using CWLDs for *in vivo* vascular imaging with visible dual-wavelength [34,35], although these experimental systems still rely on bulky and slow motorized image scanning.

For the first time, the cost-effective photoacoustic microscope (CePAM) presented herein utilizes fast laser diode scanning in reflection mode for *in situ* volumetric imaging of melanocytic lesions in murine models. System performance is enhanced by a novel application of a direct model inversion (DiMI) algorithm, enabling an extended laser-scanned field of view (FOV) using a focused transducer with high signal-to-noise ratio (SNR) and improved axial resolution for accurate depth measurements. To demonstrate the feasibility of CePAM, a variety of phantoms and chemically-induced MDTs in mice were volumetrically imaged and quantitatively compared with histopathologic analysis. The obtained results suggest that this cost-effective and noninvasive technology could ultimately guide clinicians in the early detection of melanoma through frequent screening of melanocytic skin lesions, as well as for their postoperative follow-up at the point of care.

2. Methods

2.1. Cost-effective photoacoustic microscopy system

A schematic and a photograph of the CePAM system are shown in Figs. 1a, b. The scanner primary elements include a low-cost pulsed laser diode (PLD) which is coupled to a multimode optical fiber via simple optics and powered by a current driver board. This optical assembly is encased within a portable box along with the necessary control and synchronization electronics. Then, the use of a flexible optical fiber easily transports the PLD beam from the electronics box into the movable, compact microscope head. This head incorporates two-axis laser scanning mirrors, positioned between the collimating and focusing lenses, to rapidly scan the laser spot across the imaging plane. For all phantom and *in vivo* imaging tests, the laser scan area was set to 1x1 mm^2, as limited by the aperture of the objective lens. Coaxial to the optical axis, a custom ring-shaped focused transducer receives the PA waves in reflection mode. Thus, 3D imaging is performed by 2D-laser scanning of multiple planes combined with axial mechanical scanning in discrete steps. The other two stepper motors serve as an auxiliary 2D mechanical scan either to cover larger image areas or to perform a conventional 2D confocal raster scanning. For ultrasound coupling to the sample, the transducer and the objective lens tube are immersed in water with a 3D-printed ring structure that clamps a transparent film filled with deionized water. This specifically designed water container

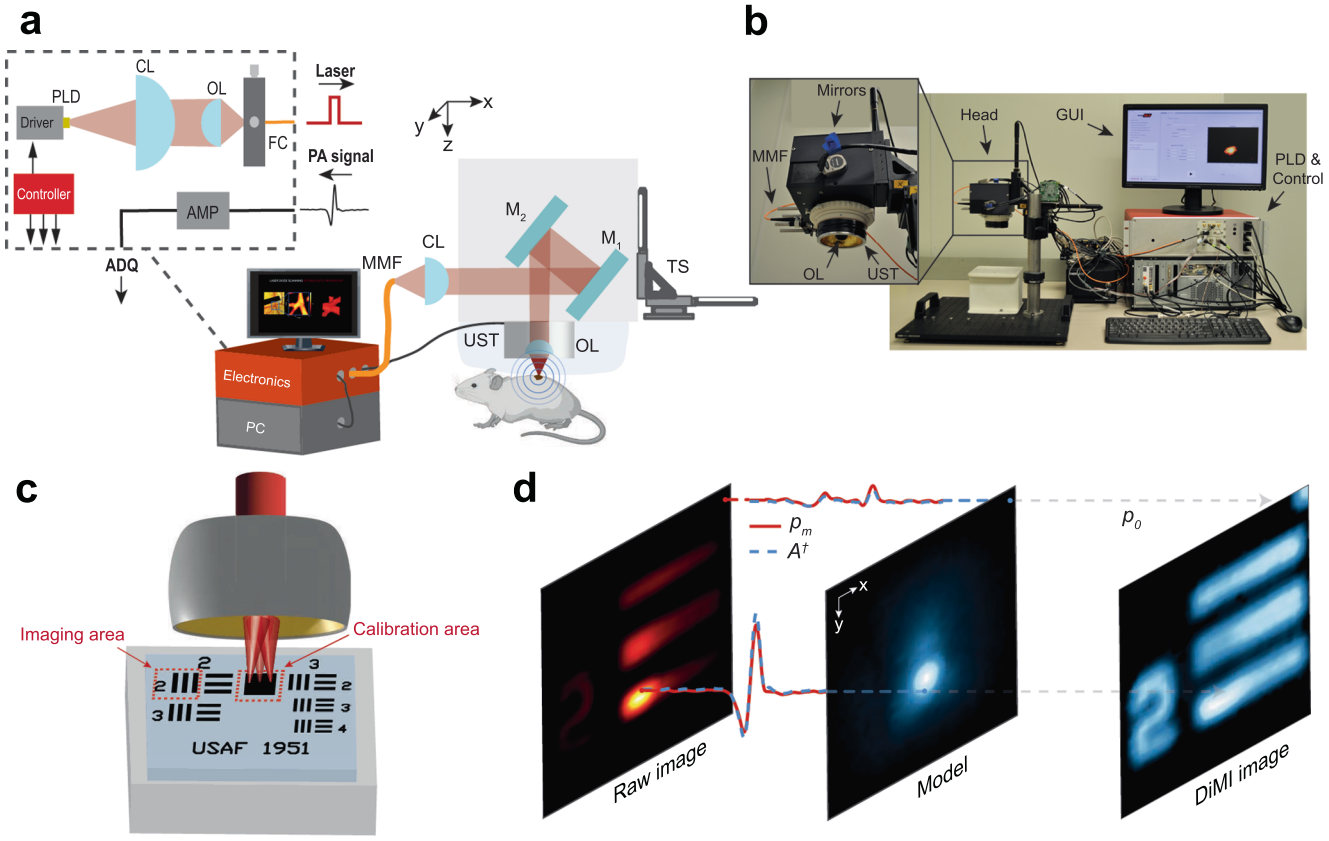

Fig. 1. CePAM laser diode scanner and the direct model inversion scheme for uniform FOV enlargement. (a) Schematic diagram of the microscope. CL: collimating lens; OL: objective lens; FC: fiber coupler; MMF: multimode fiber; M_1 and M_2: galvo-mirrors; UST: ultrasound transducer, TS: translation stages. (b) Photograph of the CePAM system. The inset depicts a zoom of the microscope head. (c) Calibration scheme of the model for the spherically focused transducer. (d) Procedure of the DiMI approach in a USAF resolution target element, where the measured PA waveform (p_m) is compared to the corresponding model calibration waveform ($A^{\dagger}$) to obtain the image pixel (p_0), thus retrieving a sensitivity-homogeneous image.

enabled reflection-mode operation on dry samples, just requiring coupling gel for efficient ultrasound transmission. Finally, the system operation is managed with an application developed in Matlab (Mathworks) running on a stand-alone computer (PC). It provides control and configuration functions through a custom graphical user interface (GUI) and communicates to the system electronics via an ethernet link. Furthermore, the rapid laser-scanned PA images are immediately displayed after processing the RF signals acquired from a PCI-express digitizer board installed in the computer.

The electronic, optical and acoustic components are described more in detail below. The laser source consists of a miniaturized pulsed laser diode (PLD) (905D2S3JT09X, Laser Components) with near-infrared emission at a 905 nm wavelength, allowing deeper penetration than visible wavelengths and rich optical contrast of melanin with respect to hemoglobin and other chromophores [35]. This laser source delivers 100 ns pulses with nominal peak power of 235 W and at a pulse repetition frequency (PRF) of up to 10 kHz, which are provided by a pulsed current driver (LDP-V 80–100, PicoLAS) and controlled by a programmable pulse generator board (PLCS-21, PicoLAS). Regarding the PA detection by the transducer, the RF signal from each laser shot is amplified (ZFL-500LN+, Minicircuits), low-pass filtered (BLP-27+, Minicircuits) and then digitized at 250 MHz sampling rate and 14-bit resolution by the PCIe digitizer board installed in the computer (ADQ14DC-2A-VG-PCIE, Teledyne SP Devices). All the triggering and synchronization events are managed by a low-cost controller board (STEMlab 125–14, Redpitaya) running a custom firmware developed in C and FPGA-Verilog.

Building on our previous optical design [33], we employed a fiber coupling strategy to homogenize the beam shape and divergence of the low-quality PLD beam, which is characterized by its large, non-uniform emitting area and high divergence. To achieve this, the PLD two-bar pattern emitting area (235x212 μm^2) is launched into a 150-μm square-core multimode fiber using two plano-convex, high-precision aspheric lenses (AL1210-B, AL2520-B, Thorlabs). On the microscope head, another set of collimating and focusing aspheric lenses (ACL2520U-B, AL1210-B, Thorlabs) serves to produce a uniform square spot of approximately 75 μm (Supplementary Information, Fig. S1), which is scanned with two-axis galvanometric mirrors (QS20XY, Thorlabs). This setup provides half-magnification of the fiber core and maintains a long working distance of 1 cm in water. This fiber-coupling design also enables resolution enhancement by placing a spatial filter (pinhole) at the fiber output, preserving both fluence and working distance with a high resolution of up to 20 μm (Supplementary Information, Fig. S1). In this work, however, we employed the standard resolution mode (without pinhole), achieving maximum energy delivery and penetration capabilities of up to 2–3 mm at mesoscopic resolution, which has been reported to be well suited for clinical dermatological applications [36–38].

The custom-made focused transducer features a central through-hole coaxially aligned to the optical tube axis. For the design of this ultrasound sensor, we optimized its geometry by maximizing the Gain-to-Focus-width Product (GFP), accounting for both optical and mechanical limitations (Supplementary Information, Fig. S2). In this work, the GFP was employed as a suitable figure of merit for the geometrical design of a focused sensor because it is independent of the frequency response, as given by its analytical expression,

$$G \times F_w = 0.7\frac{A_s}{a} = \frac{R^2}{a}(\cos\gamma_1 - \cos\gamma_2) \tag{1}$$

where A_s represents the active surface, R the spherical radius (or focal length), and a the half aperture of the transducer. This relation is simply obtained by multiplying the gain (or detection sensitivity), $G = A_s/\lambda R$ [39]; and, the Full Width at Half Maximum (FWHM) of the acoustic focus, $F_w = 0.7\lambda R/a$ [40], according to the solution of the Rayleigh-Sommerfeld integral for a focused transducer at a given acoustic wavelength λ. The right term of Eq. (1) is specifically written for a ring-shaped geometry, where the active sensor area depends on angles γ_2 and γ_1, as defined from the focal center to the edges of the aperture and the hole of the transducer, respectively. The final transducer design was manufactured by Precision Acoustics Ltd using polyvinylidene fluoride (PVdF), a highly sensitive piezo-polymer material, and featuring the following specifications: total aperture of 60 mm, focal length of 30.25 mm and central frequency of 19 MHz with a 150 % bandwidth. To select the optimal transducer frequency response, a scaled design was simulated in k-wave [41] to account for the specific pulse duration and spot size of the PLD excitation. Additionally, it is worth noting that the fabricated sensor initially showed an extreme sensitivity to external electromagnetic interference (EMI) noise, which initially buried the weak PA signals. This appeared to be due to the EMI induction on the aluminum housing, an effect that was magnified when the transducer was immersed in water. Despite most of the induced noise was mitigated by grounding the sensor with a copper braid to an adjacent metal structure, this unwanted effect necessitated more signal averaging, ultimately slowing down acquisition times.

2.2. Direct model inversion algorithm

The image field of view (FOV) of PAM systems utilizing a focused transducer and laser-scanning is typically restricted to the acoustic focus region. This is primarily due to the temporal dispersion of the spherical pulses arriving at different times at the surface of the transducer when they originate at out-of-focus locations, which eventually results in distortion of the received PA signal [19,27]. To compensate for this effect and enlarge the effective FOV beyond acoustic focus, we introduce the use of a direct model inversion (DiMI) algorithm that is computationally inexpensive.

The reconstruction of a photoacoustic image through solving the inverse problem is founded upon the assumption of a discrete physical model that accurately represents the image formation process [42]. This allows the original initial pressure value at each voxel in the image space to be recovered, based on the expected pressure signal from that position. To construct the model matrix A, the impulse responses emanating from punctual sources located at every point of the image space are captured. This process can be performed analytically, numerically, or through experimental calibration. The transducer total impulse response (TIR), which accounts for acoustic diffraction effects and bandwidth limitations [43], as well as known heterogeneities of the medium, can be introduced into the model to approximate the real system as closely as possible. The measured pressure signal p_m can be thus defined as a linear combination of the model matrix A and the initial pressure distribution p_0 as

$$p_m = Ap_0 \tag{2}$$

If A is invertible, the reconstructed image p_0^{rec}, is computed by solving the model inversion as $A^{-1}p_m$. In practice, A is singular and non-invertible in most cases, so the problem is treated as an optimization process by minimizing a cost function as [42–44]

$$p_0^{rec} = \underset{p_0 \geq 0}{\operatorname{argmin}}\{\|p_m - Ap_0\|_2^2\} \tag{3}$$

This equation can also include a regularization term if the system is ill-posed, as well as positivity constraints to ensure physical integrity. However, a simple, direct analytical solution of Eq. (2) can be defined as

$$p_0^{rec} = A^{\dagger}p_m \tag{4}$$

here $A^{\dagger}$ represents a generalized inverse, commonly referred to as the Moore-Penrose pseudoinverse, which is defined as $A^{\dagger} = (A^TA)^{-1}A^T$. In most common model-based PA tomographic scenarios with large 3D datasets, Eq. (4) becomes impractical. In these cases, iterative approaches to solve Eq. (3) such as the least-squares (LSQR) [45] are used,

which take several minutes to hours to obtain the reconstructed volume, even in fast GPU-based implementations.

However, for a PAM system with a single-element PA signal from a punctual excitation, Eq. (4) can be computed directly. In our case, this model-based method is employed to enlarge the FOV, as demonstrated with the experimental images of Figs. 1c and 1d. Here, for each laser-scanned position across the transversal focal plane, the model is a single time vector A with dimensions $1xN_s$, where N_s denotes the number of time samples. This vector captures the TIR of the transducer at that location. Therefore, each image pixel value p_0^{rec} is calculated as the scalar product of the measured signal time vector (N_sx1) and the pseudoinverse of the calibrated waveform (N_sx1). This operation can be interpreted as having two elements. First, a normalization factor that enhances the inversion output at lower signal magnitudes, thereby compensating for sensitivity loss outside the acoustic focus. Second, the scalar product of the two waveforms, which reflects the degree of similarity between these waveforms in terms of phase and morphology, and also suppresses out-of-phase components from signals originating outside the focal plane. The two-dimensional image is then formed by applying this fast procedure to every pixel scanned within the focal plane.

An important consequence for the axial depth scan is that the TIR calibration model provides remarkable selectivity of the imaging plane slice, thereby improving the accuracy of depth profiling, as quantitatively demonstrated by the experiments. This is essentially because the TIR calibration is built with A-lines from the focal plane of the transducer, so the phase-aligned signals are compensated while other off-plane signals excited by the laser depth of focus are rejected. Furthermore, the use of time-domain RF signals allows to apply complementary signal processing techniques to enhance the final volumetric image. In our system, we employed a spatially matched filter followed by a signal correlation to effectively mitigate image artifacts arising in low SNR realistic conditions.

2.3. Experimental model calibration

The TIR calibration plane was obtained experimentally using a straightforward and rapid method (Fig. 1c). We utilized a uniform and thin absorber from the square region of a commercially available USAF resolution target (R3L3S1P, Thorlabs), which is made of a 120-nm-thick chromium foil. An area of 1x1 mm^2 is scanned with a step size of 25 μm, and the signals generated at each point are averaged 500 times to obtain the matrix model waveform with low noise. The duration of the entire focal plane calibration process at a PRF of 5 kHz takes less than 2.5 min. The collected signals were stored in a 3D model matrix having n_p x n_p x n_s, where n_p is the number of pixels of the image and n_s the time samples, and then used after the imaging process for each plane of the acquired volumes in the image reconstruction process. A numerical study was also performed to obtain a simulated model using pseudo-spectral methods. To mimic the experimental conditions, both the laser excitation parameters and the transducer frequency response were considered. Due to computer memory constraints, in the simulation we utilized a scaled 3D volume that conserved the experimental spatial proportions. Additionally, a point source was scanned through only half of the focal plane, based on the assumption of a symmetric response.

2.4. System characterization

The lateral and axial resolutions of the microscope were experimentally determined by performing 2D scans on a bar pattern of the USAF resolution target. These tests were performed for the laser-scanning DiMI approach and then compared to the conventional confocal raster scanning. For both scanning methods, the lateral resolution was measured from the Edge Spread Function (ESF) across a sharp edge, and its data points fitted to obtain the Gaussian profile of the corresponding Line Spread Function (LSF). On the other hand, the axial resolution was measured from the Hilbert-transform envelope of a raw PA signal in the case of confocal raster scanning and, for the DiMI algorithm, from the ESF of a vertical scan along 1 mm travel at 25 μm steps.

Furthermore, the optical characterization of the laser diode was previously performed at several points of the laser beam transport path during the system assembly. A CCD camera with broadband vis-NIR spectral response (LT665, Ophir Photonics) was used to obtain images of the beam profile. Finally, the laser pulse energy was measured at the focal point across the full laser-scanned FOV using an integrating sphere coupled by optical fiber to a monochromator spectrometer (AvaSpec ULS2048XL-EVO, Avantes).

2.5. Phantom imaging

After model calibration, photoacoustic images of different phantoms were captured to assess the efficacy of the algorithm in an experimental environment. The performance of the DiMI algorithm was first demonstrated in a 2D test using the resolution target. It was also imaged through a 0.6-mm thick skin phantom (made by stacking silicon membranes) to test the resolution, SNR degradation and robustness of the algorithm through a highly scattering medium. In all experiments with the USAF target, the PLD was limited to about half of its full power (at PLD driver voltage 40 V) to avoid non-linear PA signal generation due to the high absorption of the thin chromium film. The PRF was set to 5 kHz, and the PA signals were averaged 50 times at each scan position. The 2D image dimensions correspond to those of the calibrated focal plane, having a pixel size of 25 μm and a total FOV of 1.2x1.2 mm^2. The 3D imaging capability of the proposed method was tested on a phantom consisting of two crossed surgical sutures (black silk, Silkam) of 250-μm diameter embedded in agar (Fig. 1f). The imaging plane area was chosen to be 1x1 mm^2, with 21 planes acquired at a vertical step size of 50 μm for a final volume of 1x1x1 mm^3. Furthermore, to measure the accuracy in depth size profiling of DiMI, confocal axial scans were performed using two rabbit blood-filled polyethylene tubes with inner diameters of 0.25 and 1 mm.

2.6. Animal preparation

All animal procedures were approved by the animal ethical committee of the *Universitat Politècnica de València* and by the Ethical Review Panel of the Directorate-General for Agriculture, Fisheries and Livestock from the Valencian Community (2024-VSC-PEA-0065) and were conducted in an accredited animal care facility (ES462500001091). Animals were maintained under a standard 12–12 h light–dark cycle at room temperature (24 ± 1°C) with normal humidity. Food and water were available ad libitum. A skin tumor mouse model (BALB/c, 7 weeks old) was induced by the topical application of two different chemicals, 7,12-dimethylbenz[a]anthracene (DMBA) and 12-O-tetradecanoyl phorbol-13-acetate (TPA) [46]. DMBA and TPA were obtained from Merck (Madrid, Spain) and were dissolved in acetone prior to topical application. The treatment was applied twice weekly to the shaved dorsal area of the mice. Topical application of DMBA/TPA to mouse skin induces the formation of dermal tumors due to the accumulation of melanocytes (nevi) [47].

2.7. In vivo imaging and histology of melanocytic dermal tumors

The CePAM system was moved to the animal facility to perform all the mice imaging tests *in situ*. Mice were weighed on a digital scale prior to dosing anesthetics and analgesic. Mice received ketamine (0.1 mg/g; 0,01 ml/g of a 10 mg/ml solution) and xylazine (0.01 mg/g; 0.005 ml/g of a 2 mg/ml solution) and buprenorphine (0.1 μg/g: 0.01 ml of a 0.01 mg/ml solution). They were picked up by the base of the tail or with a cupped hand and then briefly scuffed for injections. Anesthetics were administered intraperitoneally in the lower left or right quadrant of the

abdomen while buprenorphine was subcutaneously administered in the scruff of neck hold between the thumb and index fingers by using a 1-mL syringe and 27-gauge needle [48]. After this procedure, mice were placed under the CePAM system using a custom-made 3D printed holder that featured a square window, within which the lesion was located. To enhance the visibility of the window, the holder was covered with black tape, thus increasing the image contrast. First, a large 5x5 mm^2 PA image was acquired performing fast 1x1 mm^2 scans while moving the microscope using the motorized axes. Once the lesion was located at the correct plane, volumetric multi-plane scans were performed. For the *in vivo* experiments, the PRF was set to 8 kHz. Signals were averaged 50 times at each scan point to mitigate high induced EMI noise, obtaining the complete 1 mm^3 volume in less than 3 min. After 20 min of anesthetic induction, the mice were injected with atipamezole (0.3 mg/kg). Following the injection, they were placed in a polycarbonate cage and received thermal support for 30 min on a heating plate maintained at 46 °C. After this period, the animals were returned to their home cages.

For histology analysis, fresh skin tumor tissues were fixed in 4 % PFA, dehydrated, embedded in paraffin, and cut into 5-μm-thick sections. The sections were stained with hematoxylin for 1 min to identify the cell nucleus and eosin for 30 s to identify the cytoplasm. Finally, the sheets were dehydrated and sealed.

3. Results

3.1. Model calibration and characterization of the CePAM system

The TIR of the transducer was experimentally obtained from a laser-scanned area of 1 mm^2 on a chromium thin absorber (USAF resolution target), yielding an acoustic focus size of 150 μm at FWHM. This TIR then served as the single-plane calibration map for the DiMI algorithm, enabling a 55-fold FOV increase with respect to the acoustic focus, as demonstrated in Fig. 1d. Experimental and also numerical TIR maps, along with characteristic PA waveforms at the acoustic focus and 500 μm away from it, are supplied in Fig. S3 of the Supplementary Information.

The lateral and axial resolutions of CePAM were measured using the USAF resolution target and compared between the laser-scanning DiMI and the conventional confocal 2D raster-scanning methods. The test results are provided in Fig. S4 of the Supplementary Information. The laser-scanning DiMI achieved a lateral resolution of 49 μm (measured outside the acoustic focus), which was similar to the 47 μm resolution obtained with the confocal raster-scanning method. For the axial resolution, the confocal raster-scanning yielded a value of 275 μm which is determined by the PA signal frequency content [49]. This resolution is thus worsened due to the narrow signal spectrum typically produced by the long energy pulses (50–100 ns) of LD-based PAM systems, which are typically used to obtain sufficient PA signal levels. In contrast, the multiplane laser-scanning achieved an axial resolution of 155 μm, representing a 43 % improvement of the intrinsic axial resolution, which is attributable to the plane selectivity of the DiMI algorithm.

Fig. S1 of the Supplementary Information shows the results of the PLD beam optical characterization using a CCD camera. The PLD spectrum was measured showing a Gaussian-like profile centered at 907 nm wavelength with a 7 nm linewidth. A maximum emission pulse energy of 21.1 μJ was measured at the PLD output facet. After coupling the beam into the fiber, a pulse energy of 10 μJ was obtained at the square core fiber output. Finally, after the delivery optics in the microscope head, a 6.25 μJ pulse energy was measured at the focal spot in the center of the FOV for the PLD at the maximum voltage rating. In addition, the radial energy decay of the laser focal spot was also measured within a square area of 2x2 mm^2. Ultimately, the pulse energy was set to 4 μJ for *in vivo* imaging experiments, which yielded a mean fluence along the image FOV of 47.57 mJ cm^{-2}, considering the light attenuation introduced by the water film container. This value is below 51.4 mJ cm^{-2}, the ANSI Maximum Permissible Exposure (MPE) limit for skin irradiation at 100-ns laser pulse width and 905-nm wavelength [50].

It is important to note that the discrepancy between the measured photoacoustic lateral resolution (around 50 μm) and the optical spot size (75 μm) was most likely due to the lower LD pulse energy used for the ESF lateral resolution measurement. To avoid damaging the USAF target's thin chromium layer, the LD pulse energy was set to half of its available energy for the ESF method, while the optical spot size was measured at full energy. This lower pulse energy naturally excited fewer propagation modes inside the multimode fiber core delivering a fainter laser focal spot with a reduced PA response at its edges, thereby decreasing the ESF lateral resolution measurement.

3.2. Imaging performance of DiMI algorithm on phantoms

The 3D imaging capability of the proposed method was tested on a phantom consisting of two-crossed surgical sutures of 250 μm diameter embedded in agar (Fig. 2b). As shown in the Maximum Intensity Projection (MIP) images (Fig. 2a), the DiMI algorithm ensures a uniform SNR over the entire FOV in the top view image on the right side, while the raw image on the left is constrained to the transducer focus. For example, at a lateral offset of 500 μm from the acoustic focus center, the SNR is improved from 5.3 to 27.4 dB (Fig. 2a, white squares).

As expected from the laser excitation along its approximately 700 μm depth of focus, the raw image shows elongated objects in the cross-sectional views (Fig. 2a, bottom-left). Conversely, the suture cross-sections are reconstructed close to their actual diameter and show well-defined depth profiles when DiMI is applied with a 50 μm multi-plane step. The experimental results are presented in Fig. 1c, where the full-width suture diameter measured with DiMI yields an average value of 360 μm, compared to the 870 μm obtained from the same measurement in the raw image. For comparison with the confocal raster scanning method, an image of the same phantom was acquired. This conventional method yielded a mean suture diameter of 410 μm which is consistent with the intrinsic axial resolution of 275 μm, as determined by the characterization tests. These results demonstrate a more accurate imaging of the sample volume thickness for the multiple plane-selective scanning using the DiMI algorithm. As previously stated, this enhancement is essentially due to the TIR focal plane calibration. This calibration provides high selectivity for the PA signals of the imaging plane, effectively rejecting signal contributions excited by the laser focus depth from outside its calibrated plane.

The DiMI algorithm was tested against other fast direct model-inversion algorithms such as the spatial impulse response deconvolution [45] or spatial matched filter (SMF) [39,46] (Supplementary Information, Fig. S5). Deconvolution resulted in extremely noisy and blurred images, mainly due to the instability of the Fourier transform used to process the reconstructed signal. Conversely, the implementation of the SMF correlation led to an effective expansion of the FOV, but leading to binarized images with deteriorated lateral and axial resolution. When compared to iterative methods, the non-negative LSQR showed similar imaging performance [39,41], but within a much longer computation time of 8.4 vs. 0.8 s of DiMI.

Furthermore, the robustness of DiMI in reconstructing the image was tested through a highly scattering medium, employing the USAF resolution target with a stacked-membrane phantom of 0.6 mm thickness (Supplementary Information, Fig. S6). Although exhibiting lower resolution and SNR, DiMI still corrected the loss of sensitivity outside the 150-μm acoustic focus within a laser-scanned area of 1.2x1.2 mm^2. Finally, the accuracy of the depth profiling was determined by performing axial scans of two polyethylene tubes filled with rabbit blood (Supplementary Information, Fig. S7). From the sharp depth profiles of the multiplane DiMI method, the internal diameters of tubes with 0.25 and 1 mm were measured with much greater accuracy (0.45 and 0.9 mm) than from the stretched profiles of the raw data and also the depth-encoded A-scans. Interestingly, the irregular depth profile displayed by A-scans can be primarily attributed to the coherent interference of

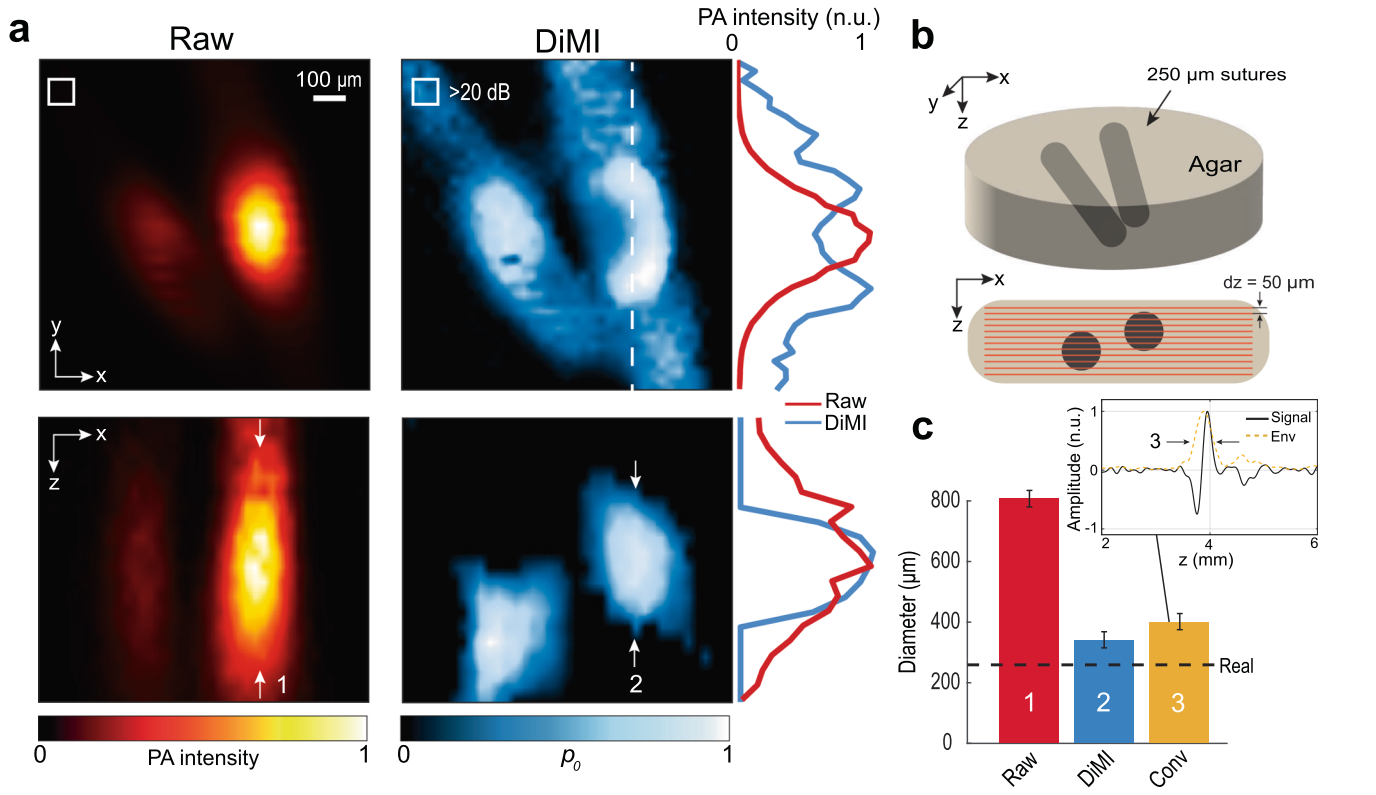

Fig. 2. (a) PA images of the two crossed black sutures phantom for comparison between DiMI algorithm (right column) and the raw data (left column) for top view (first row) and axial cross-section (bottom row). The PA intensity linear profiles are also compared on the right. The SNR values are calculated from the pixels inside the white squares. (b) Rendering of the 250 μm diameter suture phantom and axial scan 50 μm steps. (c) Diameter measurement (fullwidth mean diameter and standard deviation bar) of a suture thread from the axial profiles of 10 cross-sectional images for the raw data (1 in (a)), the DiMI approach (2 in (a)), and the conventional A-line backprojection approach from the raster scanning PAM (3, inset).

acoustic waves [47], which are simultaneously excited within the 0.7-mm-long laser depth of focus. This effect is also ruled out by the DiMI axial selective scanning.

3.3. *In vivo volumetric imaging of melanocytic dermal tumors*

The high absorption contrast of melanocytes at the selected NIR wavelength helped to demonstrate that the low-cost LD-based system presented here can be used for the anatomical characterization of MDTs, as well as of cutaneous melanoma and other pigmented skin cancers. Furthermore, the DiMI approach allows the focused transducer FOV to be extended to the laser scan area of 1 mm^2 for fast, noninvasive measurement of the tumor size and thickness with high accuracy. To demonstrate the capabilities of the CePAM scanner, we imaged three mice with MDT *in vivo*. For the first two mice, 12-dimethylbenz[a] anthracene and 12-O-tetradecanoyl phorbol-13-acetate (DMBA/TPA) induced nevus (benign dermal tumor due to the accumulation of melanocytes) [46] that can be visualized using CePAM (Fig. 3a). As shown in Fig. 3b, nevi in the first mouse are accurately imaged in three dimensions using the DiMI algorithm. The top view (*xy*) image provides anatomical information of the aggregation that correlates well with the nevi photograph, aiding in the measurement of nevi diameters and boundaries. Sagittal (*yz*) and coronal (*xz*) projections were also obtained for depth profiling. Using the data provided by CePAM, a maximum nevus thickness of 0.41 mm was determined. Fig. 3c depicts the rendered volume of the tumor using the acquired data. For clarity of visualization, a pixel connectivity function was applied to remove single bright pixels corresponding to background noise. In the 3D view are shown three melanocytic growths appearing as nevi that are located at different depths within the papule. The larger MDT having a vertical-horizontal size ratio of 2.56:1, as measured from the 3D image sections (Fig. 3b).

As shown in Fig. 3d, the DiMI approach allowed for both an extended FOV and contrast enhancement, revealing hidden aggregations that were imperceptible in the raw data image. Fig. 3e shows the transversal, coronal and sagittal projections of the nevus (red square, labeled 1) of the second mouse, obtained with CePAM and applying DiMI to each plane of the axial (*z*) scan. The same nevus was then imaged using confocal raster scanning in a single *xy*-plane to compare the two methods (Supplementary Information, Fig. S8). Multiplane laser scanning provided sharper profiles with enhanced contrast at a faster acquisition time of less than 3 min, compared to more than 12 min for mechanical raster scanning.

3.4. *In vivo slice-free characterization of melanocytic tumor thickness*

In addition to its invasive nature, histopathological analysis relies on the manual visualization of individual slices, which is a lengthy and costly diagnostic process [10]. Moreover, in the process of histological preparation, tissue samples shrink after paraffin embedding process mainly due to dehydration. A micro-CT study found that the volume reduction percentage is between 19.2–61.5 % [51], which also appears to be inversely related to tissue density. Therefore, volumetric PA imaging would be suitable to determine the actual *in vivo* tumor size and to accurately measure its Breslow depth, without waiting for biopsy sample processing [52]. To demonstrate this, a third mouse model of DMBA/TPA-induced MDT was imaged with the CePAM scanner and the results were compared with the corresponding histological cross-sectional images. Fig. 4a shows the photograph of the nevus with a visible darker pigmentation due to melanocytes (Supplementary Information, Fig. S9). The top view and depth-coded MIP images obtained from the *in vivo* 3D scan of the mouse tumor with CePAM are also shown. Despite the

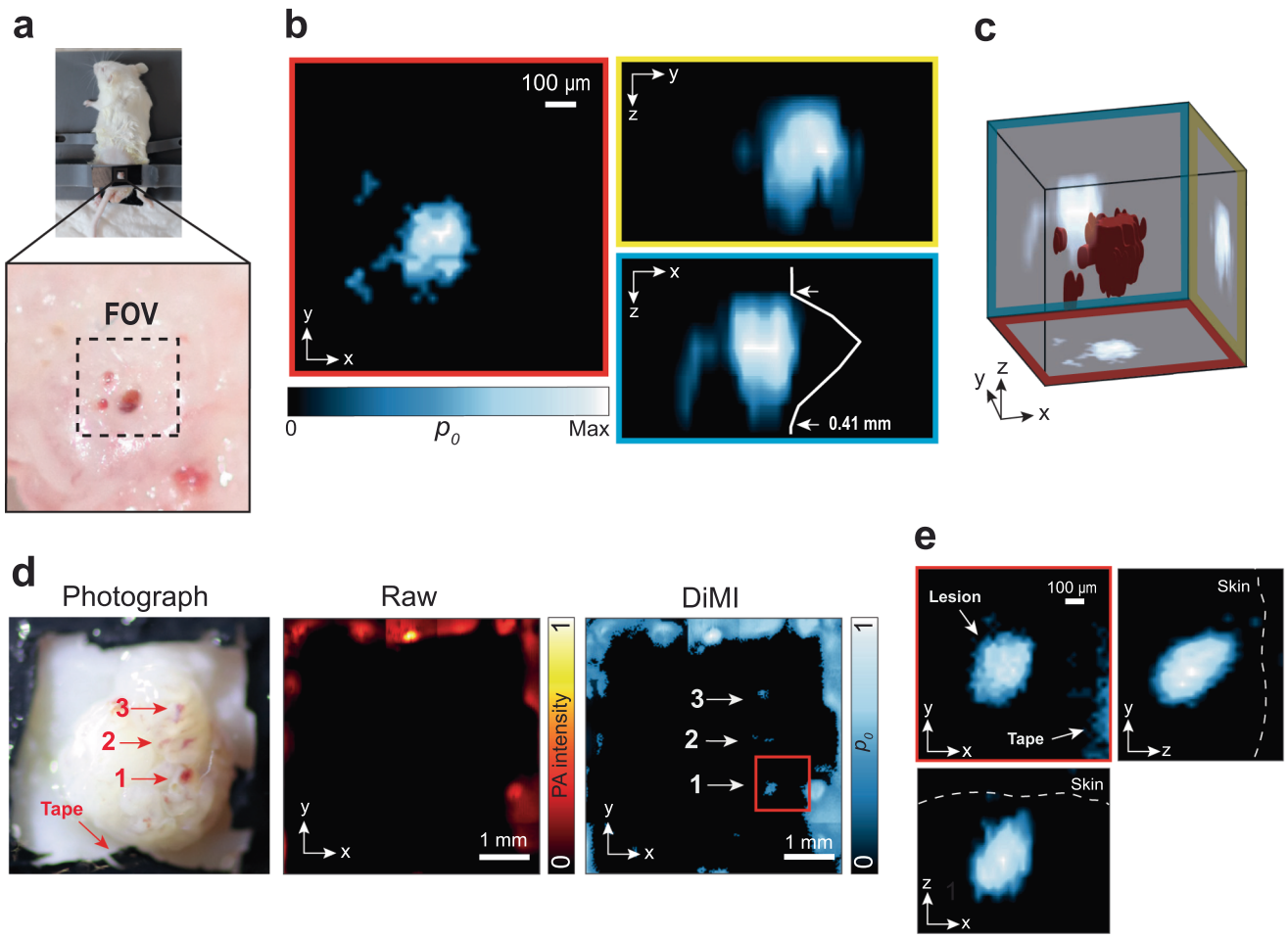

Fig. 3. CePAM images of melanocytic dermal tumors *in vivo*. (a) Photograph of the mouse with a 5x5 mm^2 window mount and close-up image of nevi, also indicating the acquired image FOV of 1 mm^2. (b) Top view (red), coronal (blue), and sagittal (yellow) MIP images of the nevi using the DiMI algorithm. The thickness of the larger nevus was measured to be 0.41 mm using the depth profile of the image. (c) Volume rendering of the imaged nevi in a 1 mm^3 volume. The 3-axis projections are displayed as shadows. (d) Photograph and PA images of the FOV during the large-area localization scan, prior to the volumetric acquisition. As observed, the DiMI algorithm shows nevi while the raw image shows only the black tape borders attached to the skin window mount. (e) 3D MIP image projections of the nevi labeled 1 in the red square area in (d).

irregular borders and surfaces of the tumor, multiplane laser scanning imaging enabled an accurate visualization of the entire lesion, as observed in the rendered volume (Fig. 4b). The tumor thickness can then be measured in any direction, so three transverse (*yz*) slices were selected from the main volume and compared with their corresponding stained histological slices (Fig. 4c). CePAM provided depth visualization of the same regions in a completely noninvasive manner, and the tumor thickness of the same 3 slices was measured from the CePAM cross-sectional images and the histological slide measurements (Fig. 4d). As expected, a greater tumor thickness is obtained from the *in vivo* acquired PA images compared to the whole slide images of the histology specimen, which shrinks due to dehydration. The processed samples show an average size reduction of 45 % with respect to the PA sections, which is consistent with the shrinkage range found in the study using the micro-CT technique [51]. For a fair comparison, we calculated the horizontal-vertical (H-V) aspect ratio of the tumor thickness, which should be the same for both, the imaging and histological techniques, assuming a uniform shrinking of the sample. As shown in Fig. 4d, the H-V ratios between both techniques are in very good agreement, and the thickest part of the tumor (0.35 mm) was easily found from the PA volumetric image at approximately its center (slice 2). These results confirm the fidelity of the CePAM system in reproducing the *in vivo* tumor volume size and suggest that cost-effective slice-free PA imaging is feasible for precise *in situ* tumor sectioning and depth assessment.

4. Discussion and conclusion

The incidence of cutaneous melanoma has steadily increased in white populations worldwide since the 1950′s [53]. While dermoscopy has revolutionized the ability to examine suspicious lesions [17], additional imaging techniques, including reflectance confocal microscopy and optical coherence tomography, can help in guiding decision-making around the need for skin biopsy [53]. However, these optical techniques provide only superficial information to the clinician. In this context, photoacoustic imaging has emerged as a promising tool for melanoma detection due to its unique ability to noninvasively image the tumor extent under several millimeters of skin and accurately measure the tumor thickness (Breslow depth), as the most important predictor of disease outcome [13,14] Moreover, once a primary melanoma is confirmed through a skin biopsy, a photoacoustic imaging device has the potential to guide less invasive and safer surgical procedures by reducing excision margins. Recognizing the lack of an affordable photoacoustic system to fully realize the advantages of this technology, we developed a cost-effective photoacoustic microscope (CePAM) to demonstrate its feasibility in mice. The CePAM system is a low-cost, optical resolution PA microscope that uses fast laser diode scanning to obtain 3D images of melanocytic dermal tumors *in vivo*.

Over the past two decades, numerous studies have been documented using various PA modalities and systems to assess melanoma Breslow

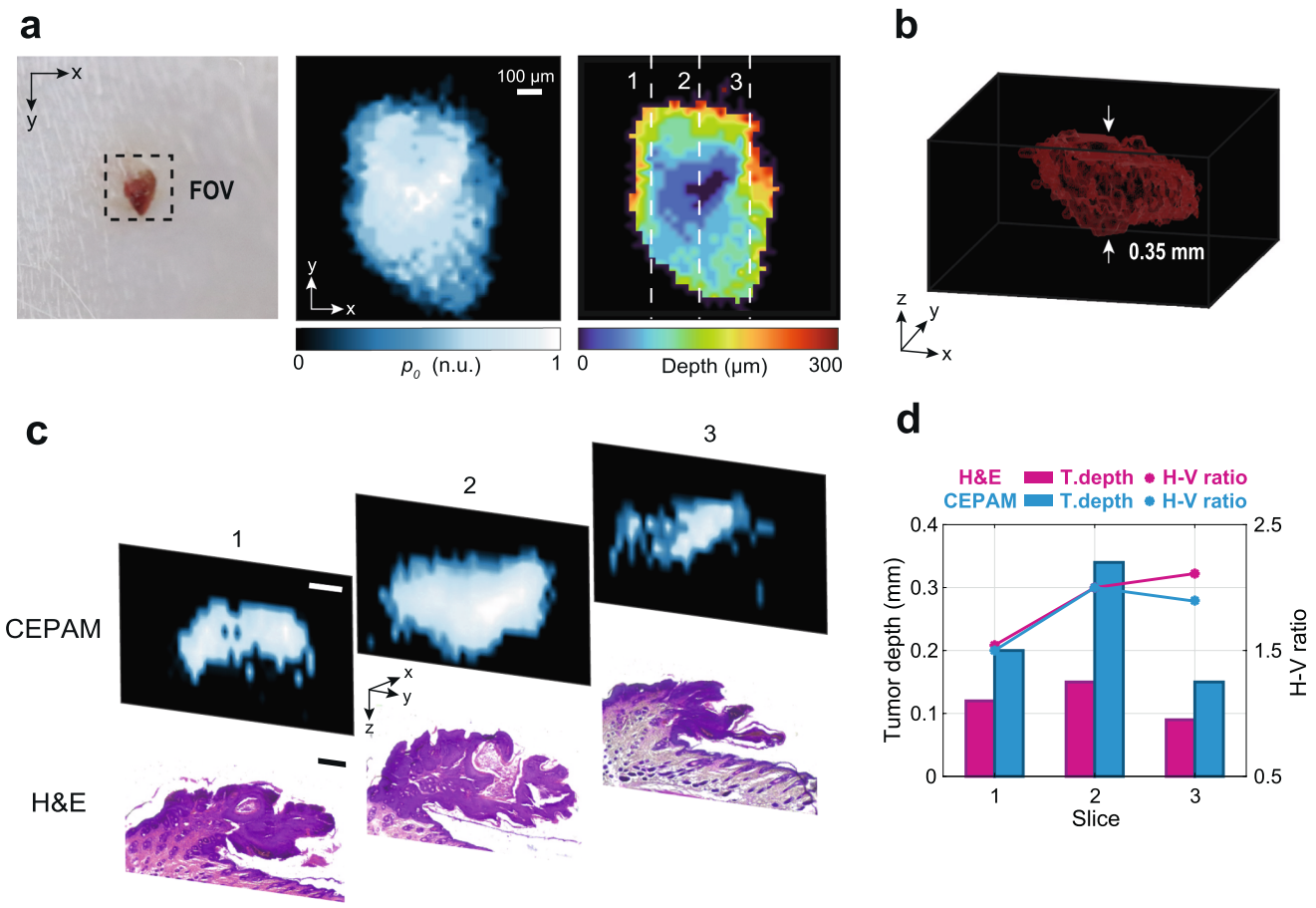

Fig. 4. *In vivo* slice-free characterization of MDT thickness using CePAM. (a) Photograph (left), top view (middle) and depth color-coded (right) PA images of the nevus. (b) Volume rendering of the imaged lesion, showing the measured central thickness of 0.35 mm. (c) Comparison between the three slice-free CePAM images (top row) and the corresponding H&E-stained sections (bottom row) at the three locations marked in (a). (d) Tumor thickness bar graph (left axis) and horizontal-vertical aspect ratio scatter plot (right axis) for CePAM and H&E comparative analysis for the three slices in (c). Scale bar 100 μm.

depth and tumor-associated angiogenesis [5–9]. Some OR-PAM systems have also been proposed for slide-free or virtual sectioning from acquired tumor images [52]. All these experimental systems have used expensive nanosecond SSLs as the laser source because of their superior performance in producing high-quality PA images. Replacing this technology with lower beam-quality LDs as the system laser source is challenging, but it would lead to a significant cost reduction of a PAM system. This is because an SSL usually represents the majority of the components' cost, while an LD source is about fifty times less expensive. Additionally, other system components, including standard optics, a single-element transducer, off-the-shelf galvo-mirrors, auxiliary motorized axes and the system's associated electronics, are also cost-effective.

Despite their low energy, LDs are particularly well suited to optical-resolution PA microscopy modality, which typically requires a few microjoules focused into a micrometer-size region. Furthermore, LDs deliver tens of kilohertz pulse repetition rates at a very compact size, with small encapsulation package and modular driver electronics, making them suitable for building affordable, fast scanning and portable PA microscopes. Then, through an effective fiber coupling strategy and a simple optical design [33], the short working distance required to achieve competitive lateral resolution with the low-quality multimode LD beams is overcome. Notably, the CePAM system enables reflection-mode imaging with a centimeter-long working distance with a lateral resolution of 49 μm.

A key feature of the system is the introduction of a direct model inversion (DiMI) algorithm. The benefits of this approach are three-fold. First, it allows to effectively extend the FOV of the transducer, which is initially constrained to its small acoustic focus. Consequently, CePAM achieves a laser-scanned area of 1 mm^2, representing a substantial increase over the 150-μm acoustic focus diameter, while maintaining a uniform response and improved SNR. Then, DiMI also provides accurate depth profiling and improved axial resolution by acting as a highly selective-plane filter of PA signals from the imaging plane, while rejecting unwanted off-plane signals excited by the laser depth of focus. The axial resolution of DiMI multiplane imaging approach outperformed the conventional raster scanning by 43 % (155 vs 275 μm). Finally, DiMI only requires a one-time, single-2D calibration map to account for the system total impulse response (TIR) waveforms across the laser-scanned imaging plane.

The imaging performance of the system was first tested on a phantom with two crossed black sutures, which provided the closest measure of the actual suture diameter (250 μm) as compared to the unprocessed raw data and the conventional image from a confocal raster scanning. Unlike direct correction algorithms that use the confocal impulse response, such as deconvolution [54] or spatial matched filter [55], DiMI accurately represents the size and shape of sutures with virtually no computational time cost. Conversely, only the iterative LSQR model-based approach [44] reaches a similar performance to DiMI, at the expense of much longer computation times, which severely hinders the implementation of real-time imaging in contrast to DiMI.

Compared to prior LD-based OR-PAM systems, which were limited by slow scanning [29,34] or transmission-mode constraints [30–32], CePAM demonstrates a unique combination of fast laser scanning in reflection mode, competitive spatial resolution and large penetration depth with cost-effective system components. The ability to image cubic millimeter volumes up to a penetration depth of 1 mm *in vivo* in less than

three minutes and produce accurate z-profiles, quantitatively validated against both phantom and histological references, is especially relevant for accurate tumor thickness measurements, highlighting its suitability for clinical or preclinical use. Importantly, CePAM accurately assessed tumor thickness in murine models of melanocytic dermal tumors, with *in vivo* measurements closely matching histology after accounting for tissue shrinkage. The aspect ratio consistency between PA and histological images supports the fidelity of the 3D reconstructions and demonstrates the capability of the system for virtual tumor sectioning, affirming its suitability for reliable noninvasive tumor assessment.

Despite these advances, the current prototype and this study present several limitations. First, DiMI substantially extended the FOV of the focused transducer to a 1x1 mm^2 laser scan area, but this was limited by the optical lens aperture, and the maximum FOV extension was not quantified at the limit of the transducer sensitivity. Second, our *in vivo* validation of a 1-mm penetration depth, including propagation through approximately 0.5 mm of highly pigmented tumor tissue, does not establish the maximal reach of the system, as none of the chemically induced melanocytic dermal tumors shown here exceeded this thickness. Previous reports of LD-ORPAM achieving imaging depths greater than 2 mm in ex vivo models [31] suggest that the CePAM system may exceed this value. Nevertheless, feasibility of a full–scale assessment of tumor thickness based on the Breslow criteria for tumor staging, i.e., up to 4 mm, remains to be determined in future *in vivo* studies. Another shortcoming is the choice of an oversized, highly focused transducer (60-mm aperture, 30.25-mm focal length) to maximize the detection sensitivity for low-energy LD pulses, which inadvertently introduced electromagnetic interference (EMI) and forced a 50–pulse averaging in the images acquisition. Reducing the aperture or improving the shielding of the transducer could help to decrease averaging and thus acquire a full 3D image in less than the reported three minutes. On the other hand, despite its narrow focus width, this geometry offers superior sensitivity owing to the larger active surface, whereas other considered geometries had lower focus gain and were inherently restricted to tight foci (<200 μm) by the limited working distance of the system and the central hole for the optics (see Supplementary Fig. S2). If an unfocused detector is used, with sufficient active area and in a short working distance system, its response is severely penalized since it would operate in the near-field regime, where the sensitivity is significantly reduced. Moreover, the temporal dispersion of signals at out-of-focus positions occurs because different portions of the spherical wavefront reach the active surface at different times. In this context, a concave geometry provides a shorter propagation path than a planar detector. Therefore, the unfocused transducer represents the least suitable option for a clinical-oriented PAM system. Further research should be conducted to develop a more compact reflection mode design that incorporates a smaller, less focused transducer, as it would benefit from the DiMI approach and enable the reconstruction of larger images with high contrast.

In summary, these findings indicate that a near-infrared laser diode-based PA microscope, offering superior melanin penetration compared to visible light, holds significant promise as an affordable clinical device capable of accurately imaging primary cutaneous melanomas. Making this technology accessible at the point of care for routine screening of suspicious skin lesions could result in earlier melanoma diagnoses and a reduction in unnecessary biopsies. Furthermore, in cases of melanoma confirmed by skin biopsy, it could aid in better defining surgical margins and detecting residual malignant melanocytes post-surgery.

Author contributions

J.J.G.G. conceived and supervised the project. J.J.G.G., J.A.N.C and A.C. designed the system. J.A.N.C., A.A., and J.J.G.G. developed the system. F.M.J. provided facility resources and established the methods and protocols for mice imaging experiments, with L.L.R. handling animal care and preparation. J.A.N.C., A.A., F.M.J., and J.J.G.G. performed the *in vivo* imaging experiments. J.A.N.C. and A.C. implemented the image reconstruction algorithm. A.C. and J.J.G.G. supervised data analysis and F.M.J. conducted the histological analysis. F.C., J.M.B. and J.J.G.G. provided funding for the project. All authors participated in the writing and revision of the manuscript.

CRediT authorship contribution statement

Javier A. Navarro-Calvo: Writing – review & editing, Writing – original draft, Visualization, Software, Methodology, Investigation, Formal analysis, Data curation, Conceptualization. **Alejandro Cebrecos:** Writing – review & editing, Writing – original draft, Validation, Supervision, Methodology, Investigation, Formal analysis, Conceptualization. **Adrián Arándiga:** Writing – review & editing, Software, Investigation, Data curation. **Laura Lorenzo-Rebenaque:** Writing – review & editing, Resources, Methodology, Investigation. **Francisco Marco-Jiménez:** Writing – review & editing, Writing – original draft, Supervision, Resources, Methodology, Investigation. **José M. Benlloch:** Writing – review & editing, Resources. **Francisco Camarena:** Writing – review & editing, Supervision, Resources, Funding acquisition. **Juan J. García-Garrigós:** Writing – review & editing, Writing – original draft, Validation, Supervision, Resources, Project administration, Methodology, Investigation, Funding acquisition, Formal analysis, Conceptualization.

Declaration of competing interest

The authors declare that they have no known competing financial interests or personal relationships that could have appeared to influence the work reported in this paper.

Acknowledgements

This work was supported by *Agència Valenciana de Innovació* IVACE+I (INNVA1/2022/50, INNVA2/2022/11); Adrián Arándiga is grateful for the financial support from *Agencia Estatal de Investigación* (PTA2023-023871-I); Javier A. Navarro-Calvo is grateful for the financial support from *Generalitat Valenciana* (INVEST/2022/171).

Appendix A. Supplementary data

Supplementary data to this article can be found online at https://doi.org/10.1016/j.ultras.2025.107831.

Data availability

The data that support the findings of this study are available on request from the corresponding author.

References

[1] L.V. Wang, J. Yao, A practical guide to photoacoustic tomography in the life sciences, Nat. Methods 13 (2016) 627.
[2] Wenfeng Xia (Ed.), Biomedical Photoacoustics, Springer Nature Switzerland. 2024. Doi: 10.1007/978-3-031-61411-8.
[3] L.V. Wang, S. Hu, Photoacoustic tomography: in vivo imaging from organelles to organs, Science 335 (2012) (1979) 1458–1462, https://doi.org/10.1126/science.1216210.
[4] P. Beard, Biomedical photoacoustic imaging, Interface Focus 1 (2011) 602–631, https://doi.org/10.1098/rsfs.2011.0028.
[5] H.F. Zhang, K. Maslov, G. Stoica, L.V. Wang, Functional photoacoustic microscopy for high-resolution and Noninvasive in vivo imaging, Nat. Biotechnol. 24 (2006) 848–851, https://doi.org/10.1038/nbt1220.
[6] Y. Wang, D. Xu, S. Yang, D. Xing, Toward in vivo biopsy of melanoma based on photoacoustic and ultrasound dual imaging with an integrated detector, Biomed. Opt. Express 7 (2016) 279, https://doi.org/10.1364/BOE.7.000279.
[7] H. He, C. Schönmann, M. Schwarz, B. Hindelang, A. Berezhnoi, S.A. Steimle-Grauer, U. Darsow, J. Aguirre, V. Ntziachristos, Fast raster-scan optoacoustic mesoscopy enables assessment of human melanoma microvasculature in vivo, Nat. Commun. 13 (2022), https://doi.org/10.1038/s41467-022-30471-9.
[8] C. Wang, L. Guo, G. Wang, T. Ye, B. Wang, J. Xiao, X. Liu, In-vivo imaging of melanoma with simultaneous dual-wavelength acoustic-resolution-based

photoacoustic/ultrasound microscopy, Appl. Opt. 60 (2021) 3772, https://doi.org/10.1364/ao.412609.
[9] Y. Zhou, W. Xing, K.I. Maslov, L.A. Cornelius, L.V. Wang, Handheld photoacoustic microscopy to detect melanoma depth in vivo, Opt. Lett. 39 (2014) 4731, https://doi.org/10.1364/OL.39.004731.
[10] J.W. Fakhoury, J.B. Lara, R. Manwar, M. Zafar, Q. Xu, R. Engel, M.M. Tsoukas, S. Daveluy, D. Mehregan, K. Avanaki, Photoacoustic imaging for cutaneous melanoma assessment: a comprehensive review, J. Biomed. Opt. 29 (2024), https://doi.org/10.1117/1.JBO.29.S1.S11518.
[11] D. Li, L. Humayun, E. Vienneau, T. Vu, J. Yao, Seeing through the skin: photoacoustic tomography of skin vasculature and beyond, JID Innov. 1 (2021) 100039, https://doi.org/10.1016/j.xjidi.2021.100039.
[12] A. Breslow, Thickness, cross-sectional areas and depth of invasion in the prognosis of cutaneous melanoma, Ann. Surg. 172 (1970) 902–908, https://doi.org/10.1097/00000658-197011000-00017.
[13] C. Garbe, T. Amaral, K. Peris, A. Hauschild, P. Arenberger, N. Basset-Seguin, L. Bastholt, V. Bataille, V. del Marmol, B. Dréno, M.C. Fargnoli, A.-M. Forsea, J.-J. Grob, C. Höller, R. Kaufmann, N. Kelleners-Smeets, A. Lallas, C. Lebbé, B. Lytvynenko, J. Malvehy, D. Moreno-Ramirez, P. Nathan, G. Pellacani, P. Saiag, A.J. Stratigos, A.C.J. Van Akkooi, R. Vieira, I. Zalaudek, P. Lorigan, European consensus-based interdisciplinary guideline for melanoma. Part 1: diagnostics: update 2022, Eur. J. Cancer 170 (2022) 236–255, https://doi.org/10.1016/j.ejca.2022.03.008.
[14] J.E. Gershenwald, R.A. Scolyer, Melanoma Staging: American Joint Committee on Cancer (AJCC) 8th Edition and Beyond, Ann Surg Oncol 25 (2018) 2105–2110. Doi: 10.1245/s10434-018-6513-7.
[15] S.N. Lo, R.A. Scolyer, J.F. Thompson, Long-term survival of patients with thin (T1) cutaneous melanomas: a breslow thickness cut point of 0.8 mm separates higher-risk and lower-risk tumors, Ann. Surg. Oncol. 25 (2018) 894–902, https://doi.org/10.1245/s10434-017-6325-1.
[16] D.L. Morton, J.F. Thompson, A.J. Cochran, N. Mozzillo, O.E. Nieweg, D.F. Roses, H. J. Hoekstra, C.P. Karakousis, C.A. Puleo, B.J. Coventry, M. Kashani-Sabet, B. M. Smithers, E. Paul, W.G. Kraybill, J.G. McKinnon, H.-J. Wang, R. Elashoff, M. B. Faries, Final trial report of sentinel-node biopsy versus nodal observation in melanoma, N. Engl. J. Med. 370 (2014) 599–609, https://doi.org/10.1056/NEJMoa1310460.
[17] J. Dinnes, J.J. Deeks, N. Chuchu, L. Ferrante di Ruffano, R.N. Matin, D.R. Thomson, K.Y. Wong, R.B. Aldridge, R. Abbott, M. Fawzy, S.E. Bayliss, M.J. Grainge, Y. Takwoingi, C. Davenport, K. Godfrey, F.M. Walter, H.C. Williams, Dermoscopy, with and without visual inspection, for diagnosing melanoma in adults, Cochrane Database Syst. Rev. (2018), https://doi.org/10.1002/14651858.CD011902.pub2.
[18] S. Jeon, J. Kim, D. Lee, J.W. Baik, C. Kim, Review on practical photoacoustic microscopy, Photoacoustics 15 (2019) 100141, https://doi.org/10.1016/j.pacs.2019.100141.
[19] J. Yao, L.V. Wang, Photoacoustic microscopy, Laser Photon Rev. 7 (2013) 758–778, https://doi.org/10.1002/lpor.201200060.
[20] J. Rebling, M. Ben-Yehuda Greenwald, M. Wietecha, S. Werner, D. Razansky, Long-term imaging of wound angiogenesis with large scale optoacoustic microscopy, Adv. Sci. 8 (2021), https://doi.org/10.1002/advs.202004226.
[21] B. Huang, T.T.W. Wong, Review of low-cost light sources and miniaturized designs in photoacoustic microscopy, J. Biomed. Opt. 29 (2023), https://doi.org/10.1117/1.jbo.29.s1.s11503.
[22] M. Erfanzadeh, Q. Zhu, Photoacoustic imaging with low-cost sources: a review, Photoacoustics 14 (2019) 1–11, https://doi.org/10.1016/j.pacs.2019.01.004.
[23] P. Kalitsounakis, G. Zacharakis, G.J. Tserevelakis, Towards affordable biomedical imaging: recent advances in low-cost, high-resolution optoacoustic microscopy, J. Microsc. (2024), https://doi.org/10.1111/jmi.13378.
[24] L. Lin, P. Zhang, S. Xu, J. Shi, L. Li, J. Yao, L. Wang, J. Zou, L.V. Wang, Handheld optical-resolution photoacoustic microscopy, J. Biomed. Opt. 22 (2016) 041002, https://doi.org/10.1117/1.jbo.22.4.041002.
[25] K. Park, J.Y. Kim, C. Lee, S. Jeon, G. Lim, C. Kim, Handheld photoacoustic microscopy probe, Sci. Rep. 7 (2017) 13359, https://doi.org/10.1038/s41598-017-13224-3.
[26] L. Li, W. Qin, T. Li, J. Zhang, B. Li, L. Xi, High-speed adaptive photoacoustic microscopy, Photonics Res. 11 (2023) 2084, https://doi.org/10.1364/PRJ.499598.
[27] L. Li, C. Yeh, S. Hu, L. Wang, B.T. Soetikno, R. Chen, Q. Zhou, K. Kirk Shung, K. I. Maslov, L.V. Wang, Fully motorized optical-resolution photoacoustic microscopy, Opt. Lett. 39 (2014) 2117, https://doi.org/10.1364/ol.39.002117.
[28] Y. Zhang, J. Chen, J. Zhang, J. Zhu, C. Liu, H. Sun, L. Wang, Super-low-dose functional and molecular photoacoustic microscopy, Adv. Sci. 10 (2023), https://doi.org/10.1002/advs.202302486.
[29] L. Zeng, G. Liu, D. Yang, X. Ji, Portable optical-resolution photoacoustic microscopy with a pulsed laser diode excitation, Appl. Phys. Lett. 102 (2013) 53704, https://doi.org/10.1063/1.4791566.
[30] X. Li, V.T.C. Tsang, L. Kang, Y. Zhang, T.T.W. Wong, High-speed high-resolution laser diode-based photoacoustic microscopy for in vivo microvasculature imaging, Vis. Comput. Ind. Biomed Art 4 (2021) 1, https://doi.org/10.1186/s42492-020-00067-5.
[31] M. Erfanzadeh, P.D. Kumavor, Q. Zhu, Laser scanning laser diode photoacoustic microscopy system, Photoacoustics 9 (2018) 1–9, https://doi.org/10.1016/j.pacs.2017.10.001.
[32] M. Seeger, A. Stylogiannis, L. Prade, S. Glasl, V. Ntziachristos, Overdriven laser diode optoacoustic microscopy, Sci. Rep. 13 (2023), https://doi.org/10.1038/s41598-023-46855-w.
[33] J.J. García-Garrigós, A. Cebrecos, J.A. Navarro-Calvo, F. Camarena, A fiber-coupled laser diode design for reflection mode optical resolution photoacoustic microscopy, Ultrasonics 132 (2023), https://doi.org/10.1016/j.ultras.2023.107008.
[34] B. Huang, S.C.K. Chan, X. Li, V.T.C. Tsang, T.T.W. Wong, Deep learning-enhanced fiber-coupled laser diode-based photoacoustic microscopy for high-resolution microvasculature imaging, Laser Photon Rev. (2024), https://doi.org/10.1002/lpor.202400452.
[35] A. Stylogiannis, L. Prade, A. Buehler, J. Aguirre, G. Sergiadis, V. Ntziachristos, Continuous wave laser diodes enable fast optoacoustic imaging, Photoacoustics 9 (2018) 31–38, https://doi.org/10.1016/j.pacs.2017.12.002.
[36] J. Aguirre, C. Gasteiger, B. Hindelang, M. Seeger, A. Bereznhoi, I. Weidenfeld, U. Darsow, A.C. Stiel, S.A. Steimle-Grauer, C. Posch, T. Biedermann, V. Ntziachristos, Non-invasive characterization of melanoma depth at single-cell resolution, J. Eur. Acad. Dermatol. Venereol. (2025), https://doi.org/10.1111/jdv.20811.
[37] J. Hult, A. Merdasa, A. Pekar-Lukacs, M. Tordengren Stridh, A. Khodaverdi, J. Albinsson, B. Gesslein, U. Dahlstrand, L. Engqvist, Y. Hamid, D. Larsson Albèr, B. Persson, T. Erlöv, R. Sheikh, M. Cinthio, M. Malmsjö, Comparison of photoacoustic imaging and histopathological examination in determining the dimensions of 52 human melanomas and nevi ex vivo, Biomed, Opt. Express 12 (2021) 4097, https://doi.org/10.1364/boe.425524.
[38] A. Breathnach, E. Concannon, J.J. Dorairaj, S. Shaharan, J. McGrath, J. Jose, J. L. Kelly, M.J. Leahy, Preoperative measurement of cutaneous melanoma and nevi thickness with photoacoustic imaging, J. Med. Imaging 5 (2018) 1, https://doi.org/10.1117/1.jmi.5.1.015004.
[39] K. Beissner, Some basic relations for ultrasonic fields from circular transducers with a central hole, J. Acoust. Soc. Am. 131 (2012) 620–627, https://doi.org/10.1121/1.3664001.
[40] D. Andrés, F. Camarena, N. Jiménez, Modelizando el campo acústico generado por superficies vibrantes, Model. Sci. Edu. Learn. 15 (2022) 5–23, https://doi.org/10.4995/msel.2022.17416.
[41] B.E. Treeby, B.T. Cox, k-Wave: MATLAB toolbox for the simulation and reconstruction of photoacoustic wave fields, J. Biomed. Opt. 15 (2010) 021314, https://doi.org/10.1117/1.3360308.
[42] X.L. Deán-Ben, D. Razansky, A practical guide for model-based reconstruction in optoacoustic imaging, Front. Phys. 10 (2022), https://doi.org/10.3389/fphy.2022.1028258.
[43] W. Li, U.A.T. Hofmann, J. Rebling, Q. Zhou, Z. Chen, A. Ozbek, Y. Gong, P. Subochev, D. Razansky, X.L. Deán-Ben, Broadband model-based optoacoustic mesoscopy enables deep-tissue imaging beyond the acoustic diffraction limit, Laser Photon Rev 16 (2022), https://doi.org/10.1002/lpor.202100381.
[44] U.A.T. Hofmann, W. Li, X.L. Deán-Ben, P. Subochev, H. Estrada, D. Razansky, Enhancing optoacoustic mesoscopy through calibration-based iterative reconstruction, Photoacoustics 28 (2022), https://doi.org/10.1016/j.pacs.2022.100405.
[45] C.C. Paige, M.A. Saunders, LSQR: an algorithm for sparse linear equations and sparse least squares, ACM Trans. Math. Soft. 8 (1982) 43–71, https://doi.org/10.1145/355984.355989.
[46] H. Li, C. Brakebusch, Analyzing skin tumor development in mice by the DMBA/TPA model. In: Methods Cell Biol, Academic Press Inc., 2021: pp. 113–121. Doi: 10.1016/bs.mcb.2020.08.004.
[47] Z. Husain, M.A. Pathak, T. Flotte, M.M. Wick2, Role of Ultraviolet Radiation in the Induction of Melanocytic Tumors in Hairless Mice following 7,12-Dimethylbenz(a) anthracene Application and Ultraviolet Irradiation1, n.d. http://aacrjournals.org/cancerres/article-pdf/51/18/4964/2445454/cr0510184964.pdf.
[48] P. Bermejo-Alvarez, K.-E. Park, B.P. Telugu, Utero-tubal embryo transfer and vasectomy in the mouse Model, J. Vis. Exp. (2014), https://doi.org/10.3791/51214.
[49] J. Yao, L.V. Wang, Sensitivity of photoacoustic microscopy, Photoacoustics 2 (2014) 87–101, https://doi.org/10.1016/j.pacs.2014.04.002.
[50] American National Standards Institute, Appendix A: Laser Safety. In: Lasers and Optoelectronics, Wiley, 2013: pp. 599–603. Doi: 10.1002/9781118688977.app1.
[51] M. Senter-Zapata, K. Patel, P.A. Bautista, M. Griffin, J. Michaelson, Y. Yagi, The role of Micro-CT in 3D histology imaging, Pathobiology 83 (2016) 140–147, https://doi.org/10.1159/000442387.
[52] R. Cao, Y. Luo, J. Zhao, Y. Zeng, Y. Zhang, Q. Zhou, A. le da Zerda, L.V. Wang, Optical-resolution parallel ultraviolet photoacoustic microscopy for slide-free histology, Sci. Adv. 10 (2024). https://www.science.org.
[53] G.V. Long, S.M. Swetter, A.M. Menzies, J.E. Gershenwald, R.A. Scolyer, Cutaneous melanoma, Lancet 402 (2023) 485–502, https://doi.org/10.1016/S0140-6736(23)00821-8.
[54] T. Lu, Y. Wang, J. Li, J. Prakash, F. Gao, V. Ntziachristos, Full-frequency correction of spatial impulse response in back-projection scheme using space-variant filtering for optoacoustic mesoscopy, Photoacoustics 19 (2020), https://doi.org/10.1016/j.pacs.2020.100193.
[55] M. Seeger, D. Soliman, J. Aguirre, G. Diot, J. Wierzbowski, V. Ntziachristos, Pushing the boundaries of optoacoustic microscopy by total impulse response characterization, Nat. Commun. 11 (2020), https://doi.org/10.1038/s41467-020-16565-2.